FRONT MATTER

Title

- State-dependent predictive coding in auditory–prefrontal circuits of behaving macaques
- Predictive coding in auditory–prefrontal circuits

Authors

Haoxuan Xu,[1,2,3,4]† Peirun Song,[1,3]† Hangting Ye,[1,3]† Ana Belén Lao-Rodríguez,[5,6,8]† Qichen Zhang,[1] Yuying Zhai,[1,3] Xuhui Bao,[4] Ishrat Mehmood,[4] Hisashi Tanigawa,[4] Zhiyi Tu,[2] Lingling Zhang,[2] Xuan Zhao,[2] David Pérez-González,[5,6,7] Manuel S. Malmierca[5,6,8]* and Xiongjie Yu[1,2,3,4,9]*

Affiliations

[1] Department of Anesthesia, Women's Hospital, Zhejiang University School of Medicine, Hangzhou, Zhejiang Province, China
[2] Department of Anesthesiology, Shanghai Tenth People's Hospital, Tongji University School of Medicine, Shanghai, China
[3] Zhejiang Provincial Key Laboratory of Precision Diagnosis and Therapy for Major Gynecological Diseases, Women's Hospital, Zhejiang University School of Medicine, Hangzhou, Zhejiang, China
[4] College of Biomedical Engineering and Instrument Science, Zhejiang University, Hangzhou, China
[5] Cognitive and Auditory Neuroscience Laboratory (Lab 1), Institute of Neuroscience of Castilla y León (INCYL), University of Salamanca, Salamanca, Spain
[6] Institute for Biomedical Research of Salamanca (IBSAL), Spain
[7] Department of Basic Psychology, Psychobiology and Methodology of Behavioral Sciences, Faculty of Psychology, University of Salamanca, Spain
[8] Department of Cell Biology and Pathology, Faculty of Medicine, University of Salamanca, Spain
[9] Lead contact: Xiongjie Yu (yuxiongj@gmail.com)
† These authors contributed equally to this work
* Corresponding authors: yuxiongj@gmail.com (X.Y.), msm@usal.es (M.S.M)

Abstract

The ability to detect deviations from expected sensory input is fundamental for adaptive behavior. We recorded electrocorticographic activity from the auditory (AC) and prefrontal (PFC) cortices of behaving macaques during an auditory oddball task to probe the cortical dynamics of predictive processing. Repetition of standard tones evoked suppression and facilitation in AC and strong low-frequency (2 Hz) enhancement in PFC, accompanied by bidirectional delta-band coupling indicative of a shared predictive state. Deviant tones triggered early AC responses followed by PFC activation and increased feedforward and feedback connectivity across delta, theta, and gamma bands. Behavioral engagement amplified both prediction and prediction error signals, strengthening cortical network coordination. Together, these findings reveal a hierarchical predictive network in which the AC encodes sensory regularities and violations, while the PFC integrates predictive context in a behaviorally dependent manner.

Teaser

Brain signals in auditory and prefrontal cortex reveal how macaques anticipate sounds and detect surprising events.

MAIN TEXT

Introduction

Living organisms constantly face a storm of stimuli, yet only a few are meaningful, while most are routine and must be ignored. Detecting novelty is therefore essential for adaptive behaviors that support survival. Sensory salience depends on context and prior experience, shaping behavioral responses [1-5]. The auditory system is particularly efficient at filtering complex acoustic input into manageable representations [6-8]. At the auditory nerve, fibers exhibit spike-frequency adaptation, in which an initial burst of firing rapidly stabilizes within milliseconds to a steady-state rate, preventing overstimulation of higher centers [9,10]. Without this mechanism, neural activity would overwhelm cognitive processing. At the neuronal level, some auditory neurons reduce their firing to repeated sounds while maintaining sensitivity to novel ones—a phenomenon known as stimulus-specific adaptation (SSA) [11-24]. At the macroscopic level, mismatch negativity (MMN), an event-related potential observed in human electroencephalogram (EEG), reflects a similar mechanism of auditory deviance detection [25-28]. Together, SSA and MMN enhance auditory efficiency by selectively encoding changes in the acoustic environment.

SSA and MMN have been extensively investigated using the classical oddball paradigm in animal models, with evidence of their presence across multiple brain regions (including the auditory midbrain and cortex) and across species and arousal states [11-13,15,28-32]. Despite these advances, most animal studies have employed acoustically simple, behaviorally irrelevant sounds, leaving key gaps in understanding how prior experience shapes SSA and MMN or how these responses reflect neuronal plasticity [8,18,28,33-35]. Moreover, many findings come from passive conditions in which subjects were not engaged in cognitive or behavioral tasks, highlighting the need to explore SSA and MMN within meaningful behavioral contexts [18,28,36,37]. Non-human primates, whose auditory and cognitive systems closely resemble those of humans, offer an ideal model for such research [38-43]. Macaques, in particular, display human-like auditory abilities including speech discrimination, sound localization and sensitivity to surprising sounds, making them especially suited for investigating the neural mechanisms of novelty detection [39,44-46].

Predictive coding posits that the brain continuously generates internal models to anticipate sensory input, minimizing discrepancies between expected (top-down processing) and actual (bottom-up processing) signals through prediction error computations. Within this framework, SSA and MMN represent neural correlates of prediction errors that intensify along the auditory hierarchy, from the inferior colliculus (IC) to the auditory cortex (AC), and from primary (lemniscal) to higher-order (non-lemniscal) regions [22,32,47,48]. These findings underscore the hierarchical nature of novelty processing but provide limited insight into the interregional, long-range cortico-cortical dynamics underlying prediction and prediction error. It has been proposed that predictions and errors operate in distinct frequency bands—low (alpha/beta oscillations) frequencies for predictions and high (gamma oscillations) frequencies for errors—originating from higher and lower cortical areas, respectively [49-55]. However, direct experimental evidence remains elusive. Testing these hypotheses requires simultaneous recordings across multiple levels of the hierarchy. The AC and prefrontal cortex (PFC) are particularly suitable, as both are critically involved in novelty detection and occupy a different hierarchical order [31,50,56-60]. Yet their respective roles and interactions during predictive processing remain poorly understood. These mechanisms are essential for adaptive behavior, allowing organisms to anticipate events, detect discrepancies, and update expectations. Examining AC–PFC communication,

especially through directional metrics such as Granger causality (GC) [53,61,62], could elucidate the circuitry mediating prediction and prediction error. Understanding these processes in behaving non-human primates is crucial for advancing our knowledge of cognitive prediction mechanisms.

In this study, we investigated how the auditory and prefrontal cortices jointly implement predictive processing during active listening. Behaving macaques performed a behaviorally relevant auditory oddball task while we recorded electrocorticography (ECoG) activity simultaneously from both regions. Granger causality analyses revealed the directionality and frequency structure of interareal communication underlying prediction and prediction-error signaling. The two regions showed distinct repetition-dependent dynamics, enhanced low-frequency coupling during auditory regularity, and temporally precise prediction-error responses to deviant sounds. Critically, task engagement strongly amplified these effects, indicating that behavioral relevance sharpens both predictive and error-related representations. Together, these findings uncover a dynamic interplay between auditory and prefrontal cortices that supports context-dependent predictive coding and flexible auditory perception.

Results

Prediction during novelty detection in AC and PFC

To probe the neural and behavioral mechanisms of novelty detection, we trained two macaques to perform an auditory oddball task composed of sequential tone blocks (7–10 repetitions each). Each block ended with either a standard tone, identical to preceding tones, or a frequency deviant (Fig. 1A).

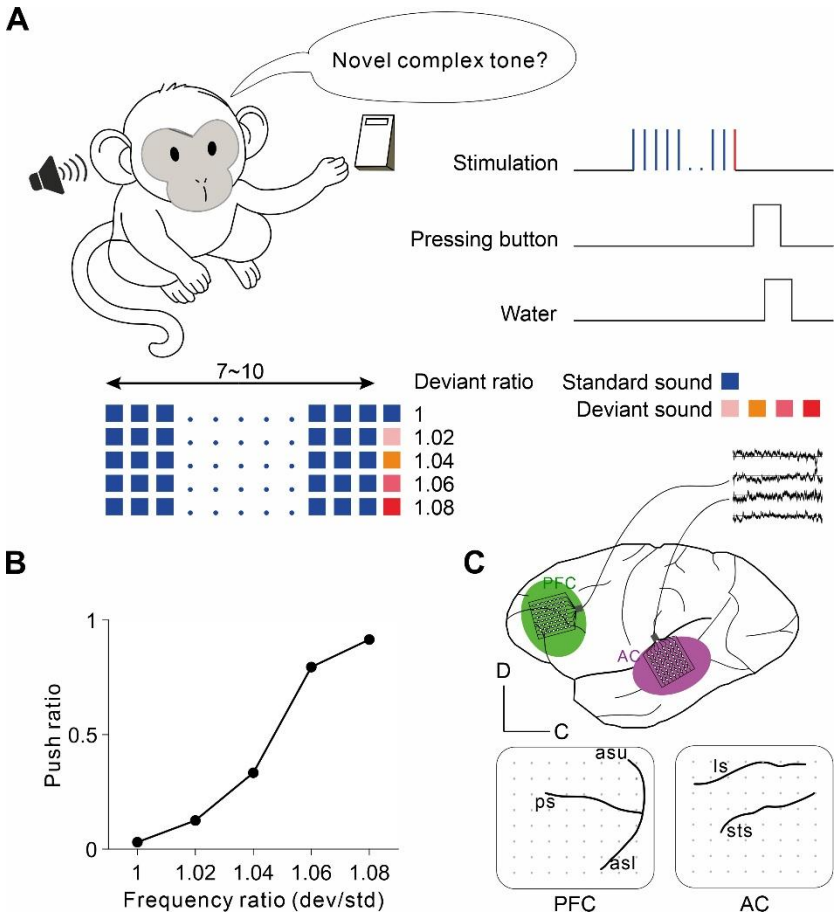

Figure 1. Experimental setup and task design for novelty detection in rhesus monkeys. (**A**) Schematic of the novelty detection task used in the experiment. The task involves presenting oddball stimuli consisting of a sequence of standard sounds (randomly ranging from 7 to 10 sounds), followed by a deviant sound, with an inter-stimulus interval (ISI) of 500 ms. The sounds are complex tones with a fixed duration of 100 ms and an intensity of 60 dB SPL. The base frequency of the deviant sound is altered relative to the standard sound by ratios of 1 (control), 1.02, 1.04, 1.06, and 1.08. The monkey is required to press a button when a deviant sound occurs or hold on in a control trial to receive a water reward. (**B**) Button press ratio as a function of the frequency ratio between the deviant and standard sounds (an example from monkey C). (**C**) Illustration of the 64-channel ECoG arrays implanted on the auditory cortex (AC) and prefrontal cortex (PFC) of monkey C (asl: arcuate sulcus lower limb; asu: arcuate sulcus upper limb; ps: principal sulcus; ls: lateral sulcus; sts: superior temporal sulcus; C: caudal; D: dorsal).

Monkeys were required to press a button within 600 ms after deviants (hit trials) and to withhold responses to standards (correct rejections). Behavioral accuracy increased with the magnitude of frequency contrast or deviation (Fig. 1B). Neural activity was simultaneously recorded from two 64-channel ECoG arrays implanted over the AC and PFC cortices (Fig. 1C; Supplementary Fig. 1 shows electrode coverage and anatomical landmarks, including the superior temporal sulcus and lateral sulcus).

We first examined neural responses to repeated standard tones and identified two distinct adaptation profiles. In the first, exemplified by an AC site, strong responses to the initial tone progressively attenuated across repetitions (Fig. 2A, top).

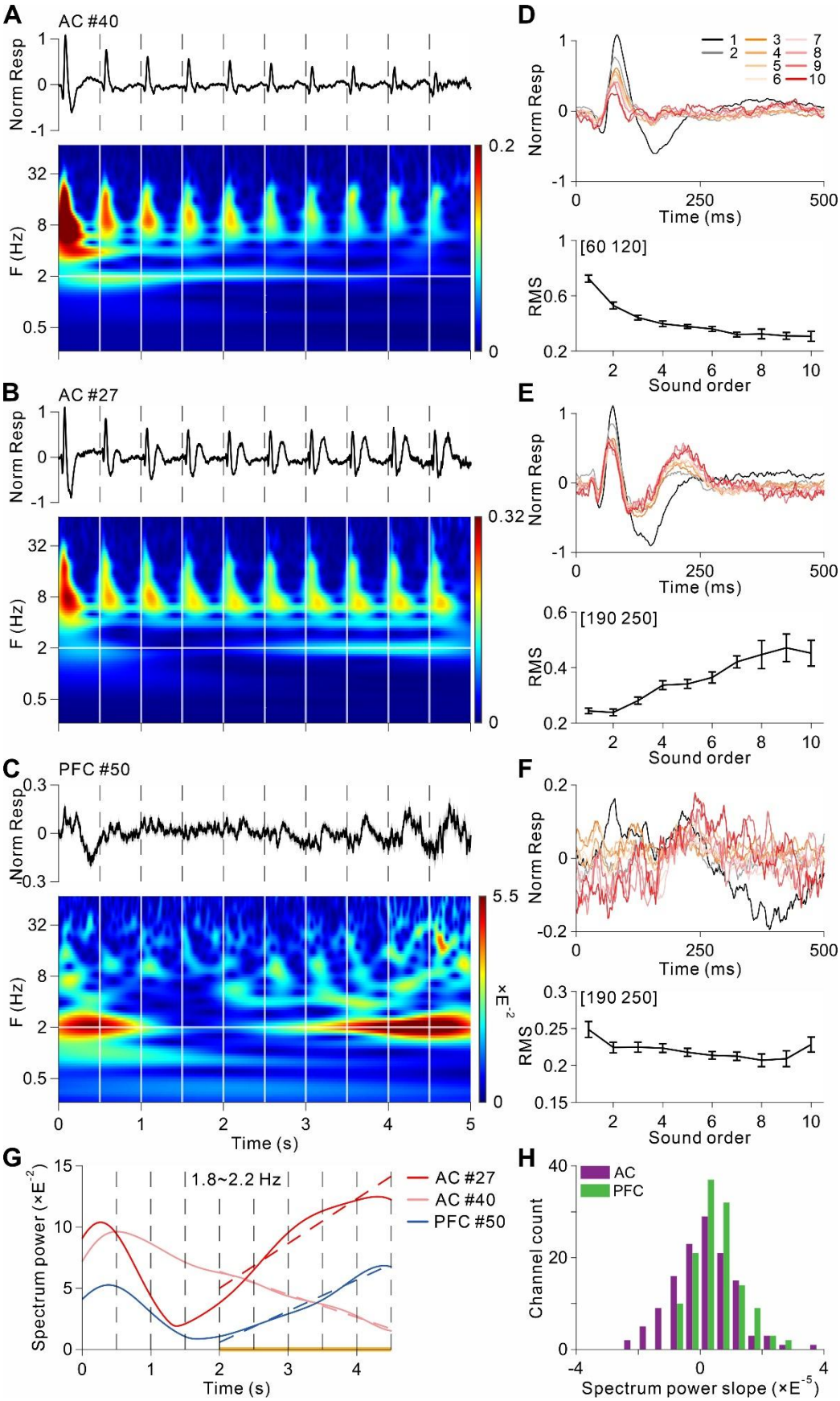

Figure 2. Suppression and enhancement of prediction in the AC and PFC of the monkey. (**A**) Example AC channel (#40) from monkey X showing prediction suppression. The top panel shows the normalized response averaged across trials, while the bottom panel

shows the corresponding time-frequency response, where color represents spectrum power. Vertical dashed lines indicate the onset of each standard sound, and the horizontal dashed line marks the 2-Hz frequency corresponding to the 500-ms ISI. (**B-C**) Example channels (B: AC #27, C: PFC #50) from monkey X showing prediction enhancement. (**D-F**) Top: normalized responses of standard sounds from orders 1 to 10 for the three example channels. Bottom: root mean square (RMS) of the responses as a function of sound order (over the time window on the top-left). (**G**) Spectrum power in the 2-Hz frequency band (1.8-2.2 Hz) for the example channels, showing changes over time. Vertical black dashed lines indicate the onset of sounds. Slanted dashed lines represent linear fits from 2 to 4.5 s (corresponding to orders 5 to 9, indicated by the horizontal yellow line). (**H**) Histogram of the slopes from the linear fits in (G) for all channels in the AC and PFC for both monkeys.

This site showed continued attenuation through the tenth repetition, consistent with predictive suppression (repetition suppression), a reduction in neural response under high certainty of repeated input [63]. Time-frequency analysis revealed parallel decreases in power around 10 Hz and 2 Hz (Fig. 2A, bottom). In contrast, a second response type exhibited progressive enhancement in amplitude from the third to tenth tone (Fig. 2B, top), accompanied by rising ~2 Hz oscillatory power aligned with the stimulus rhythm (Fig. 2B, bottom). This pattern suggests predictive facilitation (repetition enhancement), reflecting the buildup of temporal expectations or short-term memory of the tone sequence [64]. Finally, a representative PFC site showed minimal responses to early repetitions (3–6) but strong activation during later ones (8–10), paralleled by increased ~2 Hz power (Fig. 2C), indicating that prediction-related dynamics also emerged in frontal regions.

To further characterize repetition-related dynamics, we aligned neural responses by presentation order. In the example AC site, evoked activity around 100 ms after tone onset progressively declined with repetition (Fig. 2D). In contrast, a second AC site (Fig. 2E) and a PFC site (Fig. 2F) showed increasing responses centered near 220 ms. These divergent profiles reveal systematic, site-specific modulation by repetition—decreasing activity in one AC site, increasing in another, and monotonic enhancement in PFC. Corresponding time–frequency maps showed parallel trends, particularly within the ~2 Hz band (bottom rows in Figs. 2A–C).

We quantified these effects by tracking power in the 1.8–2.2 Hz band, aligned with the 2 Hz stimulation rhythm corresponding to the 500-ms ISI (Fig. 2G). Linear fits (dashed lines, Fig. 2G) across the 5th–10th tones revealed a negative slope for the first AC site, consistent with predictive suppression, and positive slopes for the second AC and PFC sites, consistent with predictive facilitation. Across sites, 57% of AC and 76% of PFC channels showed increasing 2-Hz power over repetitions (Fig. 2H). The average slope of 2-Hz power was significantly steeper in PFC than in AC ($F(1,254) = 14.22$, $p < 0.001$, $\eta^2 = 0.05$; two-way ANOVA), indicating stronger low-frequency entrainment with repetition in PFC. Together, these results show that predictive facilitation dominates in prefrontal regions, reflected in the temporal buildup of low-frequency neural activity.

After characterizing local responses to standard tones, we next examined large-scale interactions between AC and PFC during the repetition period using Granger causality analysis. We focused on the 1–3 s window of each tone block (third–seventh tones) and averaged signals across all 64 electrodes per region (Fig. 3A).

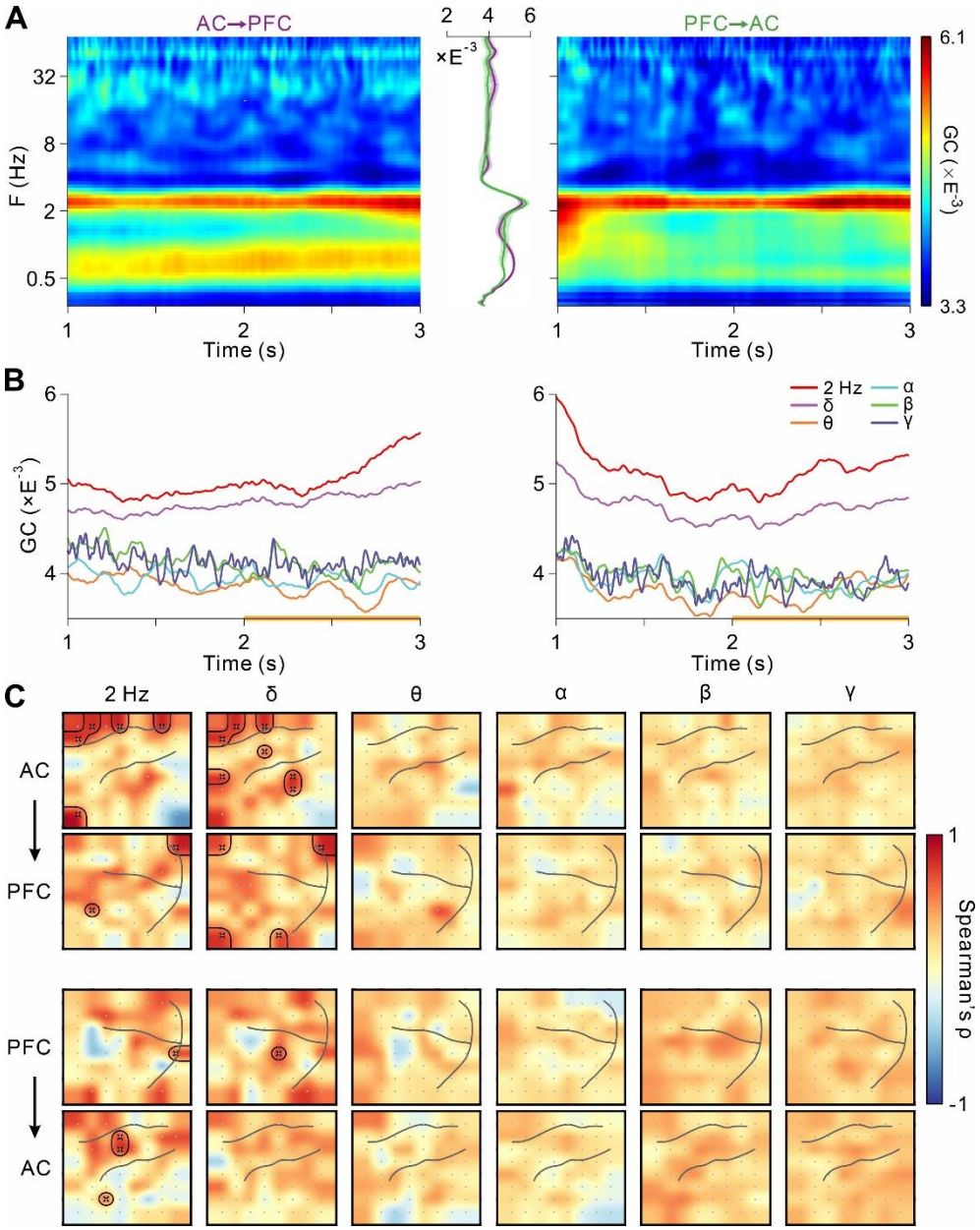

Figure 3. Enhancement of 2-Hz information flow between AC and PFC in prediction. (**A**) Time-frequency maps of Granger Causality (GC) spectrum, aligned to the onset of the first standard sound and averaged across all channels for monkey C. The example GC was computed using trials with a standard sound number of 8. Traces on the right and left display the GC averaged across time from 1 to 3 s, with a peak around 2 Hz. (**B**) GC for different frequency bands as a function of time, averaged across all channels for monkey C in both directions. Horizontal yellow bars indicate time window (2–3 s, orders 5–6) used for correlation calculation. (**C**) Topographic maps of GC correlation over time under each frequency band for monkey C. Channels with significant correlation are circled in black and marked with 'x' (Spearman's rank correlation, $p < 0.05$, false discover rate [FDR] corrected for channels).

GC spectra revealed a prominent ~2 Hz peak in both directions (AC→PFC and PFC→AC) indicating bidirectional coupling aligned with the stimulus rhythm.

To assess frequency-specific communication, we computed GC across canonical bands (2 Hz, delta: 0.6–4 Hz; theta: 4–8 Hz; alpha: 8–14 Hz; beta: 14–30 Hz; gamma: 30–70 Hz)

(Fig. 3B). In both, AC→PFC (bottom-up) and PFC→AC (top-down) directions, connectivity was strongest at 2 Hz and within the delta range, with minimal coupling at higher frequencies. Temporal correlations of GC (Spearman, 2–3 s window) confirmed that significant, stable interactions emerged exclusively in the 2 Hz and delta bands (Fig. 3C). These effects were consistent across animals (Fig. 3C and Supplementary Fig. 3). Notably, when the repetition rate was increased to 2.5 Hz, GC peaks remained near 2 Hz (Supplementary Fig. 4A), suggesting that delta-band coupling reflects an intrinsic resonance of the AC–PFC circuit rather than simple entrainment to stimulus timing.

Prediction-error during novelty detection in AC and PFC

Next, we analyzed neuronal responses to deviant tones in both AC and PFC. An example AC site showed robust deviant responses whose magnitude scaled with the frequency difference from standards (Fig. 4A).

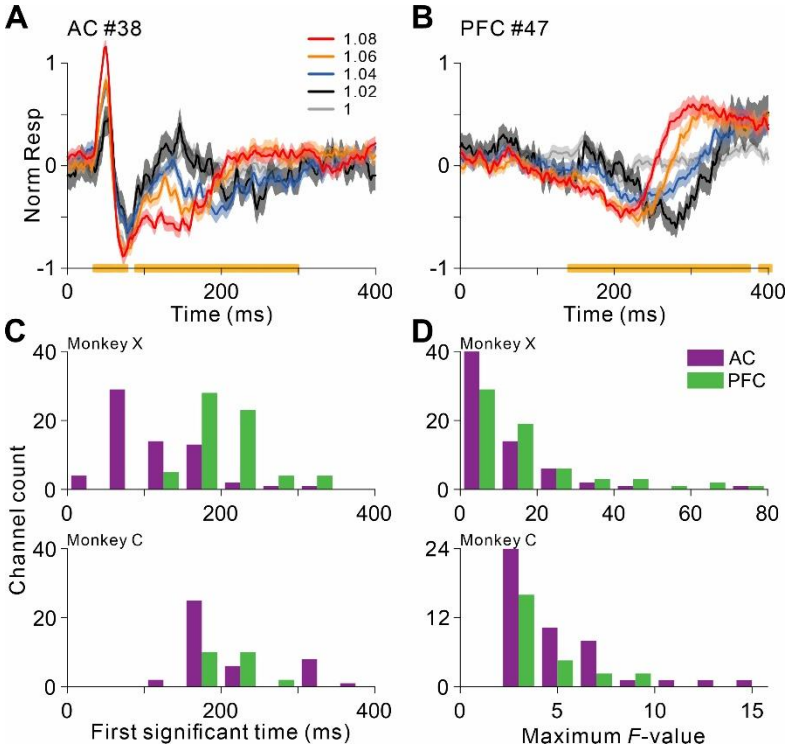

Figure 4. Prediction-error in the AC and PFC of the monkey. (**A**) Normalized responses for channel 38 in the AC of monkey X under five frequency ratios, aligned to the onset of the last sound and averaged across trials. Yellow bars at the bottom indicate significant differences among the 5 traces (permutation test, $p < 0.05$, FDR corrected for channels and time bins). (**B**) Same as (A) but for channel 47 in the PFC of monkey X. (**C**) Histogram of time bins when the five traces start to show significant differences for each channel. The AC showed faster predictive error than PFC (two-way ANOVA: $p < 0.001$ between areas, $p < 0.01$ between monkeys). (**D**) Histogram of F-values averaged from 0 to 350 ms for each channel. No significant difference was found between areas for both monkeys (Kruskal-Willis test: $p = 0.13$ for monkey X, $p = 0.2$ for monkey C).

In contrast, a representative PFC site exhibited minimal activity to standards but strong activation to deviants (Fig. 4B). To quantify these effects, we extracted two measures: (1) the first significant time, defined as the earliest time bin showing a significant deviant–standard difference in a cluster-based permutation test, and (2) the maximum F-value before 350 ms, indexing prediction-error strength. In the illustrated AC site, the first

significant time occurred at 38 ms with a maximum *F*-value of 20.93, whereas in the PFC site, significance emerged later at 144 ms with a peak *F*-value of 14.27.

At the population level, deviant–standard differences emerged reliably earlier in AC than in PFC for both monkeys (Fig. 4C; monkey X: $Z = 7.67$, $p < 0.001$, $r = 0.68$; monkey C: $Z = 2.32$, $p = 0.02$, $r = 0.29$; two-tailed Mann–Whitney U test, AC vs. PFC). In contrast, maximum *F*-values did not differ significantly between regions (Fig. 4D; monkey X: $Z = 1.48$, $p = 0.14$, $r = 0.13$; monkey C: $Z = 0.68$, $p = 0.49$, $r = 0.09$). Sorting channels by first significant time further confirmed earlier deviance detection in AC (Supplementary Figs. 5A, B). Spatial maps of maximum *F*-values revealed heterogeneous distributions within both AC and PFC, suggesting localized or tonotopic organization of prediction-error signaling (Supplementary Figs. 5C, D).

To probe functional connectivity during deviant processing, we applied Granger causality analysis. Time-frequency GC spectra (aligned to stimulus onset and averaged across channels in monkey X) revealed weak directional coupling during standards (Fig. 5A, top) but a marked GC increase for deviants (1.08 frequency ratio; Fig. 5A, middle).

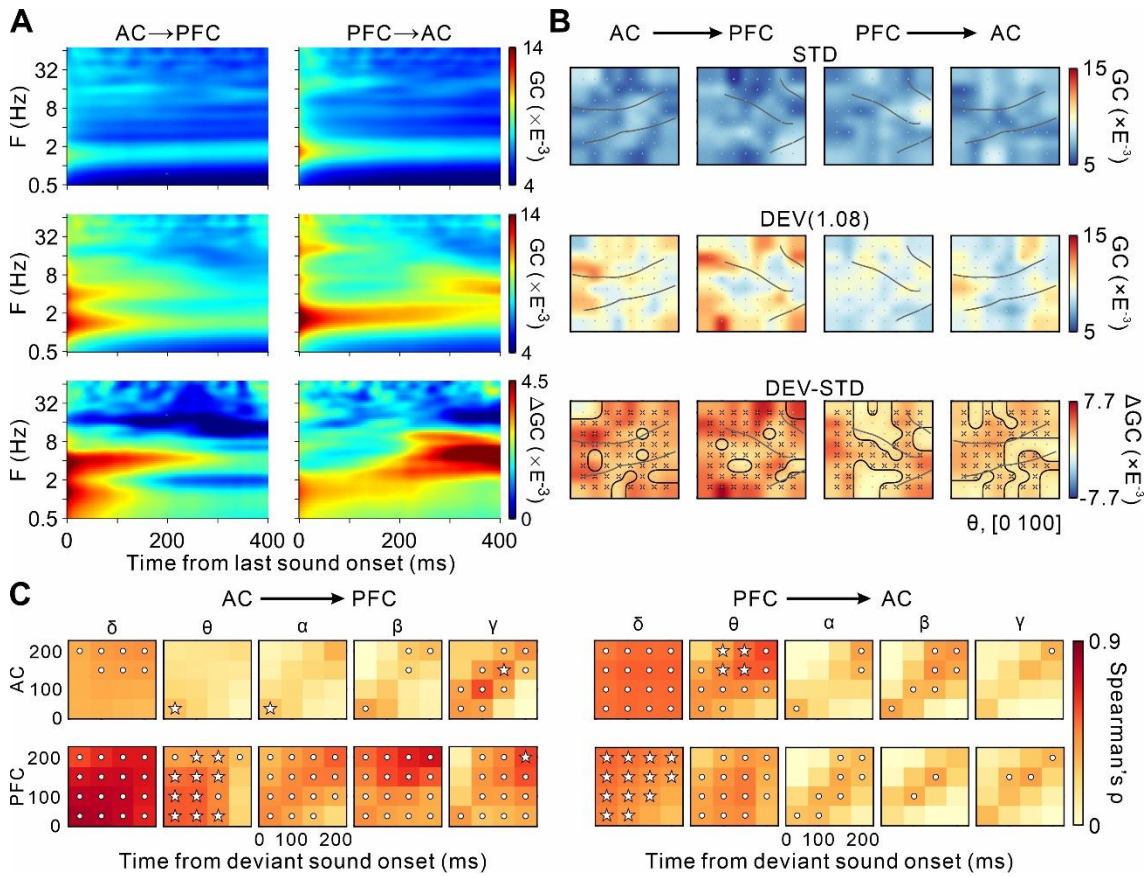

Figure 5. Information flow of prediction-error between the AC and PFC of the monkey. (**A**) Time-frequency maps of GC spectrum, aligned to the onset of the last sound and averaged across all channels for monkey X. Left: from AC to PFC. Right: from PFC to AC. Top: last sound as standard sound. Middle: last sound as deviant sound with a frequency ratio of 1.08. Bottom: differential GC (deviant 1.08 subtracted by standard). (**B**) Topographic GC maps for standard (top), deviant (middle), and differential (bottom) conditions, averaged in the theta band and the [0 100] ms time window. Channels with significant differences between responses to deviant and standard sounds are circled in black and marked with 'x' (one-tailed permutation test, $p < 0.05$, FDR corrected for

channels). (**C**) Averaged cross-period correlation matrices of differential topographic GC maps between pairs in frequency ratios of 1.04, 1.06, and 1.08 for monkey X. The color scale indicates Spearman's ρ. Significant correlations for all pairs are indicated by dots for one monkey and by stars for both monkeys (Spearman's rank correlation, $p < 0.05$, uncorrected).

This enhancement emerged within 100 ms, dominated by delta/theta activity (0.6–8 Hz, AC→PFC), and shifted to theta/alpha frequencies (4–14 Hz, PFC→AC) around 200–300 ms (Fig. 5A, bottom), indicating rapid, frequency-specific engagement of the AC–PFC network during prediction-error signaling.

Topographic GC maps corroborated these effects (Fig. 5B): bidirectional coupling was minimal for standards but rose sharply for deviants, particularly in the AC→PFC direction, with subtraction maps confirming the strongest increases along this pathway. Across frequency bands, significant information flow spanned delta to gamma ranges in both directions and in both monkeys (Supplementary Fig. 6). Temporal correlation matrices of GC values across 64 channels and frequency-ratio pairs (1.04 vs. 1.06, 1.04 vs. 1.08, 1.06 vs. 1.08) further showed robust AC→PFC interactions in the theta/alpha (4–14 Hz) and gamma (30–70 Hz) bands, while PFC→AC coupling predominated in the delta and theta (4–8 Hz) ranges (Fig. 5C). These connectivity patterns were reproduced in the second monkey (Supplementary Fig. 7), confirming dynamic, bidirectional coordination between auditory and prefrontal cortices during deviant detection.

Behavioral relevance enhances prediction and prediction-error dynamics in AC and PFC

After establishing the neural signatures of prediction and prediction error during novelty detection, next we asked how these processes were modulated by behavioral engagement. We compared neural activity between an active condition, in which monkeys performed the novelty detection task, and a passive condition, in which they heard identical auditory sequences without any task demands.

We first examined predictive processing. In the behavioral condition, a representative PFC site displayed robust ~2 Hz oscillatory activity between 3.5 and 5 s (Fig. 6A, left), which was markedly reduced during passive listening (Fig. 6A, right).

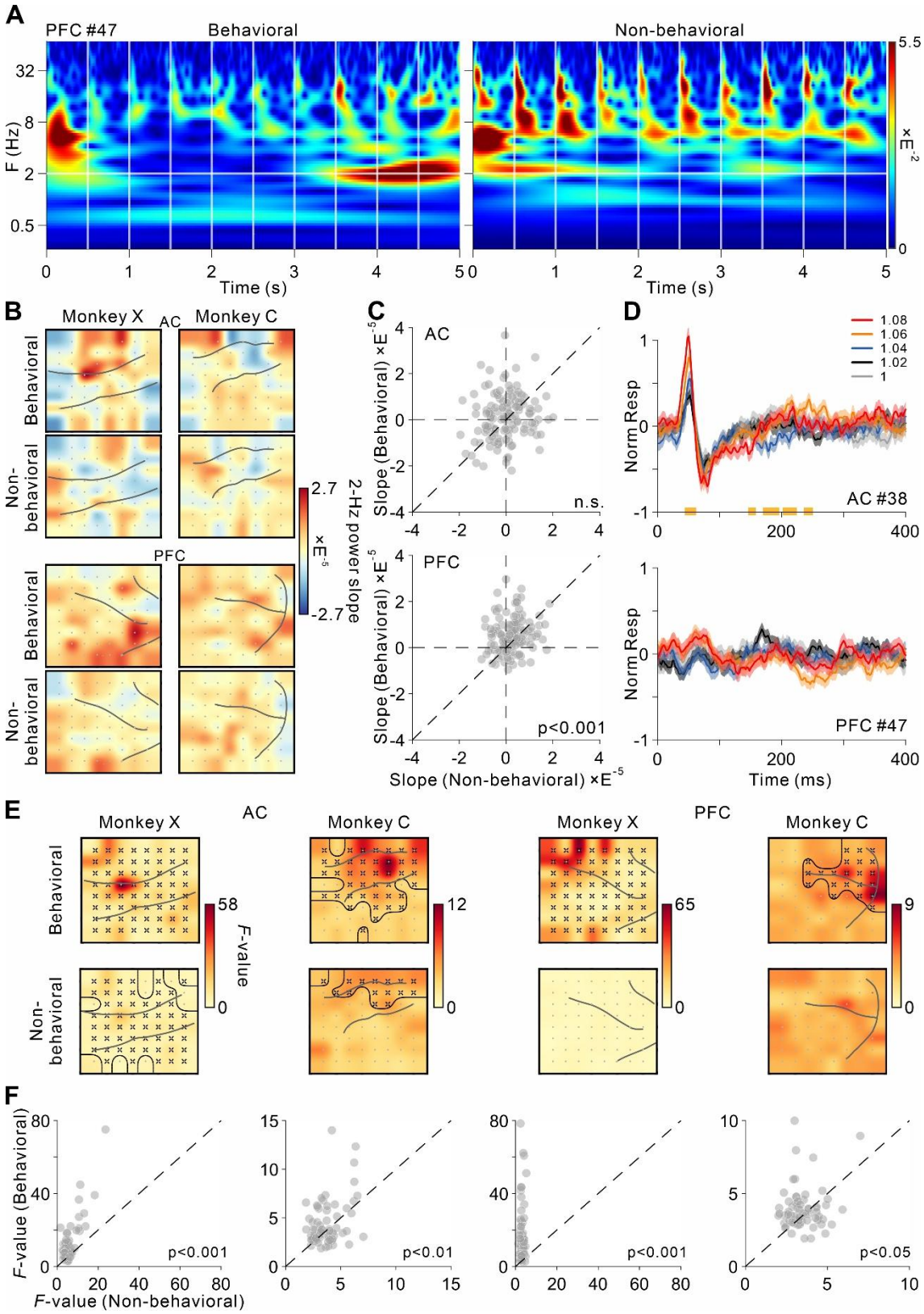

Figure 6. Behavioral context modulates prediction and prediction-error. (**A**) Time-frequency response of an example PFC channel during standard stimulus presentation under behavioral (left panel) and non-behavioral (right panel) contexts. (**B**) Topographic maps show the slopes of linear fits of 2-Hz power against time bins (from 5th to 9th standard sounds) in AC and PFC under different contexts for both monkeys. (**C**) Scatterplots comparing slopes of 2-Hz power under behavioral and non-behavioral

context, with each circle representing one recording site. The results of both monkeys are plotted together. Two-way ANOVA showed a main effect of behavioral context in PFC ($p < 0.001$) but not in AC (n.s., nonsignificant). No main effect of monkey was found for both areas. (**D**) Normalized responses for example channels from monkey X (same channel displayed in Figs. 4A-B) under five frequency ratios, aligned to the onset of the last sound and averaged across trials. Yellow bars at the bottom indicate significant differences among the 5 traces (permutation test, $p < 0.05$, FDR corrected for channels and time bins). No significant difference was found in PFC. (**E**) Topographic maps of maximum F-values within 350 ms post-stimulus for two areas for both monkeys. Channels with significant difference (< 350 ms) are circled in black and marked with 'x'. (**F**) Scatterplots comparing maximum F-values under behavioral and non-behavioral contexts, with areas and monkeys aligned with (E). Two-tailed paired t-test showed significant increase of F-values under behavioral context for both areas and monkeys—AC of monkey X: $t(63) = 5.47$, $p < 0.001$, $d = 0.68$; AC of Monkey C: $t(63) = 2.51$, $p < 0.05$, $d = 0.31$; PFC of monkey X: $t(63) = 6.68$, $p < 0.001$, $d = 0.84$; PFC of monkey C: $t(63) = 2.1$, $p < 0.05$, $d = 0.26$.

To assess regional specificity, we compared all 64 recording sites within each area (Fig. 6B). Behavioral modulation of prediction-related activity was stronger in PFC than in AC, as shown by site-by-site scatter plots (Fig. 6C). Statistical analysis confirmed a significant behavioral effect in PFC ($F(1,126) = 12.45$, $p < 0.001$, $\eta^2 = 0.05$; Fig. 6C, bottom), but not in AC ($F(1,126) = 1.43$, $p = 0.23$, $\eta^2 = 0.01$; Fig. 6C, top). Granger causality analysis further revealed weaker AC–PFC connectivity during passive listening (Supplementary Fig. 8A) compared with active engagement (Fig. 3A). Unlike the pronounced bidirectional dynamics observed during task performance, temporal modulation of connectivity was largely absent under passive conditions (Supplementary Fig. 8B).

We next examined prediction-error signaling. Example sites in both AC and PFC (Fig. 6D, left and right) showed markedly reduced differentiation between deviant and standard tones during passive listening, compared with the clear response separation observed during active task performance (cf. Figs. 4A, B). Across both regions and animals, the tonotopic distribution of F-values was attenuated in the passive condition (Fig. 6E). Site-wise comparisons confirmed significantly stronger prediction-error responses during active behavior ($p < 0.05$ for all comparisons; two-tailed paired t-test; Fig. 6F). Granger causality analysis nonetheless revealed residual AC→PFC information flow in the theta and alpha bands, indicating that basic feedforward signaling persisted even without behavioral engagement (Supplementary Fig. 9).

Discussion

In this study, we examined how the auditory and prefrontal cortices cooperate to detect and predict sensory novelty in the auditory cortex and prefrontal cortex of behaving macaques. Repetition of standard tones produced two distinct response profiles: while some AC sites showed repetition suppression, most AC and PFC sites exhibited repetition enhancement, dominated by low-frequency (~2 Hz) oscillatory activity (Figs. 2A–G). Linear fits of delta-band power confirmed stronger facilitation in PFC than in AC (Fig. 2H). Granger causality analyses revealed robust bidirectional coupling between the two cortical regions, peaking near 2 Hz within the delta band, consistent with coordinated predictive signaling (Fig. 3; Supplementary Figs. 3–4). Deviant tones elicited early responses in AC and later activation in PFC (Figs. 4A–C), with comparable prediction error magnitudes across the cortical network (Fig. 4D). Deviance processing further increased AC→PFC information flow in

the delta and theta bands and induced frequency-specific cross-cortical coupling, delta–theta from AC to PFC and delta–gamma from PFC to AC (Fig. 5A; Supplementary Figs. 6–7). Importantly, both predictive and error related responses were amplified during active engagement, showing enhanced repetition facilitation, cross-cortical connectivity, and deviance sensitivity compared with passive listening (Fig. 6; Supplementary Figs. 8–9). Together, these results support a distributed, state-dependent model of predictive coding in which the AC encodes early sensory regularities and violations, whereas the PFC integrates behavioral context to shape top-down modulation.

Dual modes of prediction in the AC–PFC circuit

Repetition suppression and repetition enhancement repetition enhancement represent complementary forms of predictive plasticity within the auditory–prefrontal network. In the AC, repetition suppression—observed in ~43% of electrodes—appeared as a gradual attenuation of evoked responses to repeated tones (Figs. 2A, D), consistent with predictive coding models in which redundant input reduces prediction-error signaling in primary auditory and subcortical nuclei [4,5,63,65]. The remaining AC sites, however, exhibited pronounced repetition enhancement, with evoked amplitudes and phase-locked power at the stimulation rhythm (~2 Hz) increasing monotonically across repetitions (Figs. 2B, E). Similar facilitation reported in marmoset and mouse AC [66,67] may represent a transient "prediction template" that sharpens temporal expectancy through delta-phase alignment [68]. The PFC showed the same dual motifs but was strongly biased toward enhancement: 76% of electrodes displayed progressive facilitation, typically with a later buildup than in AC (Figs. 2C, F–H). This predominance accords with evidence that medial PFC broadcasts precision-weighted predictions to increase auditory gain under high behavioral relevance [48,69] and sustains cross-modal predictive templates during working memory [69].

Interestingly, these predictive effects were strongly modulated by behavioral state. During passive listening, repetition enhancement strength declined sharply in PFC (33% reduction in the average 2-Hz power slope relative to the active condition) and more moderately in AC (22%), accompanied by weakened low-frequency PFC–AC coupling (Supplementary Fig. 8). This pattern mirrors evidence that task engagement amplifies frontal contributions to sensory processing [70,71], suggesting that PFC-driven repetition enhancement refreshes predictive templates during active behavior. In contrast, repetition suppression predominated under passive conditions, reflecting efficient suppression of redundant input and reduced resource allocation. This state dependence highlights a functional dissociation repetition suppression within the AC–PFC circuit: repetition suppression optimizes coding efficiency for predictable repetitive stimuli, whereas repetition enhancement enhances the representation of behaviorally relevant information through active cortical buffering.

Converging human magnetoencephalogram (MEG) and functional magnetic resonance (fMRI) work indicates that such dual repetition effects are a general feature of auditory memory-trace and prediction formation. Using a roving-standard paradigm, Recasens et al. [72] showed that repetition suppression of the N1m response is accompanied by a progressive repetition enhancement of a later sustained field, and that both components contribute to the build-up of the repetition positivity and the echoic memory trace. In an event-related fMRI study, Cacciaglia et al. [73] further demonstrated that deviant sounds preceded by a longer sequence of standard tones evoke stronger Blood Oxygen Level-Dependent responses in bilateral auditory cortex, and that responses to the standards themselves show a mixture of suppression and enhancement depending on whether they predict an upcoming deviant. These findings support the view that repetition suppression primarily reflects reduced

prediction error for highly expected input, whereas repetition enhancement indexes the strengthening of short-term auditory predictions and sensory memory representations in auditory cortex.

Our macaque ECoG data extend this framework in several important ways. First, we show that repetition suppression and enhancement coexist not only within AC but also in PFC, and that their relative expression is strongly state-dependent, with enhancement dominating under active task engagement. Second, the slow build-up of low-frequency activity we observe in PFC—and in a subset of AC sites—resembles the sustained-field repetition enhancement and deviant-history effects described in human MEG and fMRI, suggesting a common mechanism whereby frontal feedback and local delta-band entrainment maintain short-term auditory predictions during regular stimulation[72,73]. Third, by combining these repetition effects with directed connectivity analyses, we show that they are embedded in a structured AC–PFC network, in which PFC feedback preferentially amplifies enhancement-related dynamics under behavioral demands. This cross-species convergence supports the notion that dual repetition mechanisms—suppression and enhancement—are a core implementation of predictive coding in the auditory system, jointly supporting efficient encoding of predictable input and robust maintenance of context-dependent expectations.

Prediction error signaling followed a clear temporal and directional hierarchy. Deviant responses appeared earlier in AC and later in PFC, consistent with feedforward transmission of sensory violations. Although overall magnitude was similar across regions, Granger causality revealed enhanced AC→PFC flow in the delta and theta bands, with cross-frequency coupling—delta–gamma from AC to PFC and delta–theta from PFC to AC (Figs. 4–5). These interactions suggest that low frequencies coordinate prediction-error transfer, while higher bands convey content-specific updates. Persistent bidirectional coupling indicates that errors not only ascend but also trigger top-down adjustments from PFC, dynamically refining auditory representations.

The coexistence of repetition suppression and repetition enhancement within the same regions supports a flexible predictive coding framework. repetition suppression in AC reflects prediction error minimization at early sensory stages, whereas repetition enhancement in PFC indexes precision-weighted model updating [63]. Delta-phase–driven repetition enhancement in AC (Fig. 2) and task-dependent facilitation in PFC (Fig. 6) suggest that temporal coding and fronto-sensory interactions jointly refine predictive accuracy. Together, these mechanisms show how the brain balances efficiency through suppression and precision through enhancement, adapting dynamically to behavioral demands via repetition suppression, repetition enhancement, and AC–PFC coordination. Future work should examine how these processes generalize to naturalistic contexts and to clinical conditions with impaired predictive processing.

The GC patterns observed during standard tone repetitions revealed a structured interplay between AC and PFC that supports predictive maintenance. Bidirectional coupling peaked near 2 Hz (Figs. 3A, B), matching the stimulation rhythm and phase-locked delta oscillations in both regions (Figs. 2G, H). This delta-band coherence indicates that AC and PFC synchronize to encode temporal regularities, with reciprocal AC→PFC and PFC→AC signaling reinforcing the stability of predictive templates. The dominance of delta frequencies in these exchanges (Figs. 3B, C) aligns with theories positing that low-frequency oscillations coordinate hierarchical predictions [49,68,74], whereby AC conveys

sensory-derived temporal structure to PFC, which in turn modulates auditory gain to emphasize behaviorally relevant patterns [48].

Task engagement strongly modulated the strength and direction of functional coupling between AC and PFC. During active performance, top-down PFC→AC influence increased markedly compared with passive listening (Supplementary Fig. 8), mirroring the higher prevalence of repetition enhancement in PFC under behaviorally relevant conditions. This asymmetry suggests that prefrontal feedback amplifies sensory predictions when sustained attention to auditory regularities is required. In contrast, passive listening reduced PFC→AC drive, shifting the balance toward bottom-up AC-driven interactions. Such flexibility accords with predictive-coding frameworks in which precision weighting—shaped by behavioral relevance—dynamically regulates the balance between top-down predictions and bottom-up sensory evidence [63,75].

The persistence of delta-band coupling across repetition rates (Supplementary Fig. 4) further underscores its role in maintaining temporal predictions. Unlike higher-frequency interactions linked to local processing or prediction-error signaling [76], delta oscillations appear to provide a scaffold for cross-cortical predictive maintenance. This interpretation aligns with evidence that delta-phase coding in AC sharpens temporal expectancy [68,77], while PFC leverages these rhythms to sustain working-memory representations [78]. Together, AC–PFC delta synchrony during repetition emerges as a dynamic *prediction loop* that stabilizes auditory regularities and optimizes processing for anticipated inputs.

Prediction-error hierarchy and AC–PFC communication

Our findings outline a hierarchical architecture for prediction-error processing in the auditory system, defined by dynamic interactions between AC and PFC. Deviant tones evoked significant responses in both regions, yet their temporal dynamics diverged: deviations from standard responses emerged ~30–100 ms earlier in AC than in PFC (Figs. 4A–C; Supplementary Figs. 5A, B). This temporal lead aligns with evidence that prediction errors originate in lower-order auditory areas before propagating to higher-order regions, consistent with hierarchical predictive processing [79,80]. Despite this early onset, the overall magnitude of prediction-error activity—indexed by peak *F*-values—did not differ significantly between AC and PFC (Fig. 4D). These results suggest that while AC rapidly flags sensory deviations, PFC contributes to their amplification and integration, linking error detection to higher cognitive functions such as attention and decision-making [81].

To clarify the directional flow of information during deviant processing, we examined connectivity dynamics across frequencies. Deviant tones triggered a rapid increase in AC→PFC coupling within the delta and theta bands, emerging within 100 ms of stimulus onset (Fig. 5A). This pattern reflects feedforward transmission of prediction-error signals from sensory to frontal regions. Shortly thereafter, enhanced PFC→AC coupling in the same frequency range indicated feedback processes likely involved in updating predictive models [79]. The strengthening of prefrontal feedback following deviant detection suggests a rapid recalibration of predictive templates, consistent with evidence linking frontal activity to expectation updating after surprising auditory events [79].

Behavioral engagement emerged as a key determinant of prediction-error dynamics.

During active task performance, both AC and PFC exhibited stronger deviant responses and broader spatial differentiation of prediction-error activity than during passive listening (Figs. 6D–F). Connectivity analyses showed enhanced delta- and theta-band coupling under

behavioral conditions, particularly in the AC→PFC direction, indicating greater feedforward transmission of errors when auditory processing was task-relevant (Supplementary Fig. 9). These results accord with frameworks in which prediction-error signaling is weighted by attention and task demands [82], highlighting behavioral relevance as a key factor shaping both the magnitude and direction of information flow across cortical networks.

Together, the data support a bidirectional model of auditory predictive processing: AC rapidly detects sensory deviations and conveys them to PFC, which integrates contextual information before sending refined predictions back to sensory cortex. This recurrent exchange promotes adaptive perception and exemplifies the hierarchical reciprocity central to predictive coding theories.

Materials and Methods

Experimental model and surgical procedures

We conducted experiments in two adult male rhesus monkeys (Macaca mulatta; subjects C and X), aged 7 years and weighing between 5.5 and 7 kg. All experimental protocols strictly complied with the Guide for the Care and Use of Laboratory Animals (Directives 86/609/EEC, 2003/65/EC, and 2010/63/EU) and the Regulations for the Administration of Affairs Concerning Experimental Animals of the People's Republic of China (GB 14925-2010), and were approved by the Bioethics Committee of Zhejiang University (ZJU20200148). Each monkey was implanted with two 64-channel subdural electrode arrays (E64-2500-50-200, NeuroNexus Technologies, USA) positioned over the left auditory cortex (AC) and prefrontal cortex (PFC). The surgical and ECoG recording procedures followed those described in our previous report[83].

Aseptic techniques were employed throughout surgery. Monkeys were premedicated with ketamine (50 mg/kg) and medetomidine (0.03 mg/kg), then intubated and maintained under anesthesia with artificial ventilation to stabilize body temperature at 37°C using an electric heating mat. Vital signs (oxygen saturation, heart rate, and end-tidal CO_2) were continuously monitored to adjust anesthesia depth as required. Each subject's head was stabilized in a stereotaxic frame (Narishige, Japan). After local infiltration with lidocaine, the scalp and overlying muscles were retracted, and a titanium headpost (Gray Matter Research, USA) was secured to the skull with bone screws and resin. Craniotomy and durotomy were performed under a surgical microscope (Carl Zeiss, Germany). Following implantation, the dura mater, bone flap, and skin were sutured, and the exposed area was covered with resin. Postoperative care included ketoprofen administration for three days and antibiotic treatment for one week to prevent infection and ensure recovery.

ECoG recording

The ECoG electrodes had a diameter of 0.2 mm and gold recording sites embedded in a 2 × 2 cm polyimide substrate. Electrode impedances measured at 1 kHz ranged from 20 to 50 kΩ, with an inter-electrode spacing of 2.5 mm. Preoperative MRI scans were used to determine the target coordinates and craniotomy size for each subject. A gold reference electrode was placed near the ECoG array within the subdural space and oriented toward the dura mater. Lead wires from both the ECoG and reference electrodes were connected to micro-connectors (ZIF-Clip 64, Tucker-Davis Technologies, USA), housed in a titanium chamber fixed to the skull with dental resin. Neural signals were amplified and band-pass filtered between 0.5 and 300 Hz using a differential amplifier (RZ5, Tucker-Davis Technologies).

Sound stimulation

All recordings were performed in a sound-attenuated chamber. Monkeys were seated in a primate chair with the head fixed, the right ear oriented toward a free-field loudspeaker (LS50, KEF, UK), and one hand resting on a response button. Acoustic stimuli were digitally generated using a computer-controlled auditory workstation (RZ6, Tucker-Davis Technologies) at a 100 kHz sampling rate and delivered through the contralateral (right) speaker. Sound pressure levels were calibrated using a ¼-inch condenser microphone (Brüel & Kjær 4954, Denmark) connected to a PHOTON/RT analyzer (Brüel & Kjær, Denmark).

The stimuli consisted of complex tones composed of six harmonics, defined by the following equation:

$$\mathrm{y}(t) = \sum_{i=1}^{6} \frac{1}{6} \sin\left[2\pi \left(2^{i} f_0\right) t\right] \tag{1}$$

where t represents time and f_0 is the base frequency of the tone. The standard sound had a base frequency of 245 Hz. For deviant tones, the base frequency was altered relative to the standard according to the ratio λ, such that $f_{\mathrm{dev}} = f_{\mathrm{std}} \times \lambda$, with λ randomly selected from 1.02, 1.04, 1.06, or 1.08. Both standard and deviant tones had a duration of 100 ms and were presented at 60 dB SPL.

Behavioral task

Monkeys were trained to perform a novelty-detection task based on an auditory oddball paradigm (Fig. 1A) [39,40,84]. Each trial began when the monkey pressed a button to initiate the sequence. Two seconds after the press, a series of 8–11 complex tones were presented at a rate of 2 Hz (500-ms inter-stimulus interval (ISI), defined as the time between sound onsets). A 5-s inter-trial interval was imposed, during which button presses were invalid.

Within each sequence, the initial tones were standards with identical frequencies, while the final tone served as the target. In deviant trials, the target tone differed in frequency from the preceding sounds, whereas in control trials it was identical. The monkey was required to press the button within 600 ms after deviant onset to receive a water reward. This response window prevented random button presses at the end of each block, since the minimum reaction time exceeded 200 ms.

Deviant trials were defined by the frequency ratio (λ) between deviant and standard tones, with λ = 1.02, 1.04, 1.06, or 1.08. Control trials corresponded to λ = 1. Each condition was presented randomly and repeated 40–50 times per recording session. The number of standards preceding the target varied randomly between 7 and 10 to prevent anticipatory responses based on sequence length.

After each behavioral session, a non-behavioral session was conducted in which a baffle was placed between the button and the monkey's hands to block any motor responses. Additionally, an extra behavioral session was recorded using a shorter ISI of 400 ms for both monkeys.

Behavioral performance was evaluated according to two criteria. First, Correct Hit (Deviant Identification): the monkey had to correctly identify the deviant sound with at least 80 % accuracy (button-press ratio > 0.8) for the largest frequency difference

condition. Second, Correct Rejection (Absence of Deviant): in control trials, the monkey had to correctly withhold responses, achieving at least 90 % accuracy (button-press ratio < 0.1). Only recording sessions meeting both criteria were included in the analyses. In total, five behavioral and four non-behavioral sessions were recorded per monkey.

Data preprocessing

ECoG data were downsampled to 500 Hz and band-pass filtered between 0.1 and 200 Hz, followed by a 50 Hz notch filter to remove line noise. The filtered signals were segmented from 3 s before to 7 s after the onset of the first sound in each trial. To reduce noise and artifact contamination, we performed independent component analysis (ICA) using the 'runica' function from the *FieldTrip* toolbox [85]. Components were visually inspected and retained or rejected based on their spatial topography and variance.

After ICA, the data were re-referenced in three consecutive steps. First, we applied common average referencing (CAR) by subtracting the mean signal across all channels within each array. This step minimized inter-array differences related to electrode impedance and array-specific properties. Second, we applied orthogonal source derivation by subtracting the average signal from the four nearest neighboring electrodes (two horizontal and two vertical). This local re-referencing reduced residual common-reference and volume-conduction effects, thereby enhancing spatial specificity. Finally, the signals were normalized by their temporal standard deviation to ensure equal weighting across electrodes and trials. The re-referenced data were then averaged across recording sessions for subsequent response comparison and time–frequency analysis.

For Granger causality (GC) analysis, we applied an additional preprocessing step to the re-referenced data. The average event-related potential (ERP) was subtracted from individual trials to remove phase-locked evoked components associated with stimulus onsets and offsets. This procedure isolated non–phase-locked, internally generated activity, such as induced oscillations, which better reflect functional interactions between cortical regions.

Time-frequency analysis

Time-frequency analysis was performed on both re-referenced and ERP-subtracted datasets using the MATLAB 'cwt' function. Morlet wavelets with a time–bandwidth product of 5 (default parameters) were used as the analytic basis functions.

For prediction analyses, the time-frequency response (TFR) during standard sound presentations was computed using the integrated ERP data. ERPs corresponding to trials with different numbers of standard sounds were calculated separately and then combined using a weighted average. To minimize edge artifacts introduced by the cone of influence (COI) in the wavelet transform, data segments were zero-padded to 10 s on both sides before transformation and subsequently trimmed to their original duration.

For Granger causality analysis, TFRs were computed at the single-trial level. Specifically, in prediction GC analysis, only the standard sound period of each trial was included, from the onset of the first tone up to the onset of the deviant tone (or one ISI after the last standard tone in control trials). For prediction-error GC analysis, TFRs were computed using the 1 s period following the onset of the final deviant or standard sound.

Prediction suppression and enhancement analysis

Prediction-related suppression and enhancement were quantified by averaging spectral power within a frequency band centered around the stimulus repetition rate (± 0.2 Hz relative to the repeat rate). This corresponded to 1.8–2.2 Hz for the 500-ms ISI and 2.3–2.7 Hz for the 400-ms ISI (Fig. 2G; Supplementary Fig. 2C). To estimate temporal changes in predictive activity, the mean spectral power at the repeat rate was fitted across the sequence of standard sounds, specifically from the 4th to the 9th tone (Fig. 2G; Supplementary Fig. 2C). The resulting slopes of these linear fits were compared between cortical regions (AC vs. PFC; Fig. 2H; Supplementary Fig. 2D), ISI conditions (400 vs. 500 ms; Supplementary Figs. 2E–F), and behavioral contexts (behavioral vs. non-behavioral; Figs. 6B–C).

Granger causality (GC) analysis

Granger causality quantifies the directional influence of one time series on another by assessing whether past values of one signal improve the prediction of future values of the other. We used a nonparametric GC approach in which the transfer matrix and residual covariance matrix were derived by factorizing the cross-spectral density (CSD) matrix. The CSD was computed from wavelet-transformed spectra for all electrode pairs between the AC and PFC.

For prediction GC analysis, all trials without button presses during the standard sound period were included, spanning from the onset of the first sound to the onset of the deviant sound (or one ISI after the last standard tone in control trials). Trials containing different numbers of standard tones (7–10) were analyzed separately. For prediction-error GC analysis, data were extracted from non-behavioral sessions and from successful behavioral trials, spanning from the onset of the final sound to 1 s post-stimulus.

Nonparametric GC values were computed bidirectionally (AC→PFC and PFC→AC) for all electrode pairs, across 72 frequency bins (0.6–70 Hz) and temporal bins (2 ms step size). Baseline GC values, obtained from the pre-stimulus period (−3 to −2.5 s relative to the first sound onset), were subtracted from subsequent results. Frequencies were grouped into five canonical bands: δ (0.6–4 Hz), θ (4–8 Hz), α (8–14 Hz), β (14–30 Hz), and γ (30–70 Hz), and GC values were averaged within each band.

To estimate the average directional information flow across cortical regions, GC maps were computed by averaging GC values between each electrode in one area (AC or PFC) and all electrodes in the other area. This was done for both directions (AC→PFC and PFC→AC), across frequency ratios (1, 1.02, 1.04, 1.06, 1.08), frequency bands, and overlapping time windows (100-ms bins with 50-ms steps).

For prediction GC, temporal dynamics of information flow were assessed by computing Spearman's rank correlations of GC values across consecutive time bins (corresponding to sound orders 5–6; 2–2.5 s for 500-ms ISI) for each electrode and standard-tone condition. Topographic maps of Spearman's ρ, averaged across conditions with 7–10 standard tones, were generated for each frequency band and direction. Electrodes showing significant correlations ($p < 0.05$, FDR-corrected across electrodes) were marked with an 'x' (Fig. 3C; Supplementary Figs. 3–4).

For prediction-error analysis, differential GC maps were constructed by subtracting the GC map for the standard condition (frequency ratio = 1) from that of each deviant condition (e.g., ratio = 1.08). To evaluate the spatial stability of these maps across deviant

conditions, we computed cross-condition correlation matrices (Fig. 5C; Supplementary Figs. 7 and 9) using Spearman's rank correlations between differential GC maps for each pair of deviant conditions (1.04, 1.06, and 1.08) within each frequency band, separately for each monkey and behavioral context. The smallest deviant condition (1.02) was excluded due to an insufficient number of successful trials. Cross-condition similarity was considered consistent when correlations reached $p < 0.05$ (uncorrected) across all deviant pairs (1.04 vs. 1.06, 1.04 vs. 1.08, and 1.06 vs. 1.08) in both animals.

Statistical analysis

Spearman's rank correlation coefficients (ρ) and right-tailed p-values were computed in two contexts: (1) to quantify temporal changes in information flow between the AC and PFC in the prediction GC analysis (Fig. 3C; Supplementary Figs. 3, 4C, 8B), and (2) to assess the topographic stability of differential GC maps across deviant conditions (Fig. 5C; Supplementary Figs. 7, 9). Two-way ANOVAs were used to test whether the slopes of linear fits of spectral power varied across brain areas, behavioral contexts, or subjects (Fig. 2H; Supplementary Fig. 2D; Fig. 6C). Effect sizes for all N-way ANOVAs were expressed as partial eta squared (η^2):

$$\eta_k^2 = \frac{SS_k}{SS_k + SS_{\text{error}}} \tag{2}$$

where k denotes the k-th factor, SS_k is the sum of squares for that factor, and SS_{error} the residual sum of squares. Values of 0.01, 0.06, and 0.14 were interpreted as small, medium, and large effects, respectively. Two-tailed Mann–Whitney U tests were used to compare the first significant time and the maximum F-values between brain regions (Figs. 4C–D). Effect size was expressed as rank-biserial correlation (r):

$$\mathrm{r} = \frac{|Z|}{\sqrt{n_1 + n_2}} \tag{3}$$

where Z is the standardized test statistic and n_1, n_2 are sample sizes of the two groups. Values of 0.1, 0.3, and 0.5 indicated small, medium, and large effects, respectively.

Two-tailed paired t-tests were applied to compare maximum F-values (Fig. 6F) between behavioral contexts. The corresponding effect size was reported as Cohen's d:

$$\mathrm{d} = \frac{\overline{X} - \overline{Y}}{\sqrt{\frac{1}{N-1}\sum_{i=1}^{N}\left(X_i - Y_i - \left(\overline{X} - \overline{Y}\right)\right)^2}} \tag{4}$$

where d represents Cohen's d. X and Y are the paired samples with a total number of N. X_i and Y_i are the ith elements from the paired samples. $\overline{X}$ and $\overline{Y}$ are mean values of the samples. A value of 0.2 for d implies a small effect, while 0.5 for a medium effect and 0.8 for a large effect.

Bayesian analyses were conducted to quantify evidence for the null hypothesis. For pairwise comparisons, we used Bayesian paired- or independent-sample t-tests with a Jeffreys–Zellner–Siow (JZS) prior [86]. For multi-level factors, Bayesian N-way ANOVA was applied using default Cauchy priors on effect sizes[87]. All Bayes factors (BF_{10}) were computed with the *BayesFactor* toolbox[88] for MATLAB, where $BF_{10} > 1$ indicated support for the alternative hypothesis and $BF_{10} < 1$ indicated support for the null.

To evaluate differences in neural responses across frequency ratio conditions (Figs. 4A–B, 6D), we applied non-parametric cluster-based permutation tests using the *FieldTrip* toolbox. This approach controls for multiple comparisons by identifying spatiotemporal clusters of

contiguous significant samples and testing their likelihood under the null hypothesis. The procedure was two-tailed ($p < 0.05$, corrected) and comprised seven steps:

1. **Data aggregation:** Event-related responses were averaged across trials for each of the five frequency-ratio conditions.
2. **First-level testing:** At each time point (and electrode), an *F*-test across conditions produced an *F*-value per sample.
3. **Neighbor definition:** Channels adjacent in orthogonal directions on the ECoG grid were defined as neighbors.
4. **Cluster formation:** Samples exceeding $p < 0.05$ (uncorrected) were grouped into spatiotemporal clusters.
5. **Cluster-level statistic:** The *F*-values within each cluster were summed to yield a cluster-level statistic.
6. **Permutation:** Condition labels were randomly shuffled 1,000 times, generating a null distribution of maximum cluster-level statistics.
7. **Significance testing:** Observed clusters were deemed significant if their statistics fell within the extreme 2.5% tails of the null distribution.

This non-parametric method effectively controlled the family-wise error rate while maintaining sensitivity to distributed temporal and spatial effects.

Finally, to assess whether mean GC values differed significantly between deviant and standard conditions, a one-tailed permutation test was performed (Fig. 6B and Supplementary Fig. 6). For each electrode and frequency band, GC values from deviant and standard trials were randomly shuffled across 1,000 permutations to generate a null distribution of differential GC values. The *p*-value was defined as the proportion of permuted values exceeding the observed difference. Electrodes were considered significant when $p < 0.05$ across all three deviant conditions (1.04, 1.06, 1.08).

All data preprocessing, time–frequency transformations, and statistical analyses were performed using custom MATLAB scripts (R2021a, MathWorks Inc.) in combination with the *FieldTrip* and *BayesFactor* toolboxes, as well as supplementary routines written in Python (v3.9). Figures were generated in MATLAB and refined in Adobe Illustrator for publication. All analyses were conducted on trial-averaged and single-trial data at the electrode level, and statistical significance was established at $p < 0.05$ unless otherwise stated.

References

1 Fritz, J. B., Elhilali, M., David, S. V. & Shamma, S. A. Auditory attention—focusing the searchlight on sound. *Current Opinion in Neurobiology* **17**, 437-455 (2007). https://doi.org/https://doi.org/10.1016/j.conb.2007.07.011

2 Carandini, M. & Heeger, D. J. Normalization as a canonical neural computation. *Nat Rev Neurosci* **13**, 51-62 (2011). https://doi.org/10.1038/nrn3136

3 Waiblinger, C., McDonnell, M. E., Reedy, A. R., Borden, P. Y. & Stanley, G. B. Emerging experience-dependent dynamics in primary somatosensory cortex reflect behavioral adaptation. *Nat Commun* **13**, 534 (2022). https://doi.org/10.1038/s41467-022-28193-z

4 Yu, X.-J., Xu, X. X., Chen, X., He, S. & He, J. Slow recovery from excitation of thalamic reticular nucleus neurons. *Journal of neurophysiology* **101**, 980-987 (2009). https://doi.org/10.1152/jn.91130.2008

5 Song, P. R. *et al.* Adaptation in the Dorsal Belt and Core Regions of the Auditory Cortex in the Awake Rat. *Neuroscience* **455**, 79-88 (2021). https://doi.org/10.1016/j.neuroscience.2020.11.042

6 Nelken, I. Stimulus-specific adaptation and deviance detection in the auditory system: experiments and models. *Biol Cybern* **108**, 655-663 (2014). https://doi.org/10.1007/s00422-014-0585-7

7 Nelken, I. Processing of complex sounds in the auditory system. *Curr Opin Neurobiol* **18**, 413-417 (2008). https://doi.org/10.1016/j.conb.2008.08.014

8 Escera, C. & Malmierca, M. S. The auditory novelty system: an attempt to integrate human and animal research. *Psychophysiology* **51**, 111-123 (2014). https://doi.org/10.1111/psyp.12156

9 Zhang, F., Miller, C. A., Robinson, B. K., Abbas, P. J. & Hu, N. Changes across time in spike rate and spike amplitude of auditory nerve fibers stimulated by electric pulse trains. *J Assoc Res Otolaryngol* **8**, 356-372 (2007). https://doi.org/10.1007/s10162-007-0086-7

10 Willmore, B. D. B. & King, A. J. Adaptation in auditory processing. *Physiological Reviews* **103**, 1025-1058 (2022). https://doi.org/10.1152/physrev.00011.2022

11 Malmierca, M. S., Cristaudo, S., Pérez-González, D. & Covey, E. Stimulus-Specific Adaptation in the Inferior Colliculus of the Anesthetized Rat. *The Journal of Neuroscience* **29**, 5483 (2009). https://doi.org/10.1523/JNEUROSCI.4153-08.2009

12 Antunes, F. M., Nelken, I., Covey, E. & Malmierca, M. S. Stimulus-specific adaptation in the auditory thalamus of the anesthetized rat. *PLoS One* **5**, e14071 (2010). https://doi.org/10.1371/journal.pone.0014071

13 Duque, D., Pérez-González, D., Ayala, Y. A., Palmer, A. R. & Malmierca, M. S. Topographic distribution, frequency, and intensity dependence of stimulus-specific adaptation in the inferior colliculus of the rat. *J Neurosci* **32**, 17762-17774 (2012). https://doi.org/10.1523/jneurosci.3190-12.2012

14 Malmierca, M. S. & Auksztulewicz, R. Stimulus-specific adaptation, MMN and predictive coding. *Hear Res* **399**, 108076 (2021). https://doi.org/10.1016/j.heares.2020.108076

15 Lao-Rodríguez, A. B. *et al.* Neuronal responses to omitted tones in the auditory brain: A neuronal correlate for predictive coding. *Sci Adv* **9**, eabq8657 (2023). https://doi.org/10.1126/sciadv.abq8657

16 Zhai, Y. Y., Sun, Z. H., Gong, Y. M., Tang, Y. & **Yu*, X.** Integrative stimulus-specific adaptation of the natural sounds in the auditory cortex of the awake rat. *Brain structure & function* **224**, 1753-1766 (2019). https://doi.org/10.1007/s00429-019-01880-2

17 Zhai, Y. Y. *et al.* Synaptic Adaptation Contributes to Stimulus-specific Adaptation in the Thalamic Reticular Nucleus. *Neuroscience bulletin* **224**, 1753-1766 (2020). https://doi.org/10.1007/s00429-019-01880-2

18 Song, P., Zhai, Y. & **Yu*, X.** Stimulus-specific adaptation (SSA) in the auditory system: Functional relevance and underlying mechanisms. *Neurosci Biobehav Rev* **149**, 105190 (2023). https://doi.org/10.1016/j.neubiorev.2023.105190

19 Rui, Y. Y., He, J., Zhai, Y. Y., Sun, Z. H. & **Yu*, X.** Frequency-Dependent Stimulus-Specific Adaptation and Regularity Sensitivity in the Rat Auditory Thalamus. *Neuroscience* **392**, 13-24 (2018). https://doi.org/10.1016/j.neuroscience.2018.09.015

20 Gong, Y. *et al.* Cross-Modal Interaction and Integration Through Stimulus-Specific Adaptation in the Thalamic Reticular Nucleus of Rats. *Neuroscience bulletin* (2022). https://doi.org/10.1007/s12264-022-00827-8

21 Ulanovsky, N., Las, L. & Nelken, I. Processing of low-probability sounds by cortical neurons. *Nat Neurosci* **6**, 391-398 (2003). https://doi.org/10.1038/nn1032

22 Nieto-Diego, J. & Malmierca, M. S. Topographic Distribution of Stimulus-Specific Adaptation across Auditory Cortical Fields in the Anesthetized Rat. *PLOS Biology* **14**, e1002397 (2016). https://doi.org/10.1371/journal.pbio.1002397

23 Pérez-González, D., Lao-Rodríguez, A. B., Aedo-Sánchez, C. & Malmierca, M. S. Acetylcholine modulates the precision of prediction error in the auditory cortex. *Elife* **12** (2024). https://doi.org/10.7554/eLife.91475

24 Pérez-González, D. *et al.* Deviance detection in physiologically identified cell types in the rat auditory cortex. *Hearing Research* **399**, 107997 (2021). https://doi.org/https://doi.org/10.1016/j.heares.2020.107997

25 Bussey, T. Novelty in the brain. *Trends in Cognitive Sciences* **3**, 126 (1999). https://doi.org/10.1016/S1364-6613(99)01305-4

26 Fitzgerald, K. & Todd, J. Making Sense of Mismatch Negativity. *Front Psychiatry* **11**, 468 (2020). https://doi.org/10.3389/fpsyt.2020.00468

27 Tiitinen, H., May, P., Reinikainen, K. & Näätänen, R. Attentive novelty detection in humans is governed by pre-attentive sensory memory. *Nature* **372**, 90-92 (1994). https://doi.org/10.1038/372090a0

28 Nelken, I. & Ulanovsky, N. Mismatch Negativity and Stimulus-Specific Adaptation in Animal Models. *Journal of Psychophysiology* **21**, 214-223 (2007). https://doi.org/10.1027/0269-8803.21.34.214

29 Fishman, Y. I. & Steinschneider, M. Searching for the Mismatch Negativity in Primary Auditory Cortex of the Awake Monkey: Deviance Detection or Stimulus Specific Adaptation? *Journal of Neuroscience* **32**, 15747-15758 (2012).

30 Taaseh, N., Yaron, A. & Nelken, I. Stimulus-specific adaptation and deviance detection in the rat auditory cortex. *PloS One* **6**, e23369 (2011). https://doi.org/10.1371/journal.pone.0023369

31 Casado-Román, L., Carbajal, G. V., Pérez-González, D. & Malmierca, M. S. Prediction error signaling explains neuronal mismatch responses in the medial prefrontal cortex. *PLOS Biology* **18**, e3001019 (2020). https://doi.org/10.1371/journal.pbio.3001019

32 Parras, G. G. *et al.* Neurons along the auditory pathway exhibit a hierarchical organization of prediction error. *Nature Communications* **8**, 2148 (2017). https://doi.org/10.1038/s41467-017-02038-6

33 Grimm, S., Escera, C. & Nelken, I. Early indices of deviance detection in humans and animal models. *Biol Psychol* **116**, 23-27 (2016). https://doi.org/10.1016/j.biopsycho.2015.11.017

34 Yaron, A., Jankowski, M. M., Badrieh, R. & Nelken, I. Stimulus-specific adaptation to behaviorally-relevant sounds in awake rats. *PLoS One* **15**, e0221541 (2020). https://doi.org/10.1371/journal.pone.0221541

35 Shiramatsu, T. I. & Takahashi, H. Mismatch-negativity (MMN) in animal models: Homology of human MMN? *Hear Res* **399**, 107936 (2021). https://doi.org/10.1016/j.heares.2020.107936

36 Farley, B. J., Quirk, M. C., Doherty, J. J. & Christian, E. P. Stimulus-specific adaptation in auditory cortex is an NMDA-independent process distinct from the sensory novelty encoded by the mismatch negativity. *J Neurosci* **30**, 16475-16484 (2010). https://doi.org/10.1523/jneurosci.2793-10.2010

37 Erlbeck, H., Kübler, A., Kotchoubey, B. & Veser, S. Task instructions modulate the attentional mode affecting the auditory MMN and the semantic N400. *Frontiers in Human Neuroscience* **Volume 8 - 2014** (2014). https://doi.org/10.3389/fnhum.2014.00654

38 Du, X. *et al.* The multifaceted role of the inferior colliculus in sensory prediction, reward processing, and decision-making. *Elife* **13** (2025). https://doi.org/10.7554/eLife.101142

39 Gong, Y. *et al.* Neural correlates of novelty detection in the primary auditory cortex of behaving monkeys. *Cell Rep* **43**, 113864 (2024). https://doi.org/10.1016/j.celrep.2024.113864
40 Du, X. *et al.* Protocol for behavioral and neural recording in macaques during a novelty detection task. *STAR Protoc* **5**, 103252 (2024). https://doi.org/10.1016/j.xpro.2024.103252
41 Xu, X., Yu, X., He, J. & Nelken, I. Across-ear stimulus-specific adaptation in the auditory cortex. *Frontiers in neural circuits* **8**, 89 (2014).
42 Ye, H. *et al.* Hierarchical Temporal Processing in the Primate Thalamocortical System: Insights from Non-Linguistic Structured Stimuli. *Research* (2025).
43 Song, P. *et al.* A new function of offset response in the primate auditory cortex: marker of temporal integration. *Communications Biology* **7**, 1350 (2024).
44 Tsunada, J. & Cohen, Y. E. Neural mechanisms of auditory categorization: from across brain areas to within local microcircuits. *Front Neurosci* **8**, 161 (2014). https://doi.org/10.3389/fnins.2014.00161
45 Tsunada, J., Lee, J. H. & Cohen, Y. E. Representation of speech categories in the primate auditory cortex. *Journal of neurophysiology* **105**, 2634-2646 (2011). https://doi.org/10.1152/jn.00037.2011
46 Woods, T. M., Lopez, S. E., Long, J. H., Rahman, J. E. & Recanzone, G. H. Effects of Stimulus Azimuth and Intensity on the Single-Neuron Activity in the Auditory Cortex of the Alert Macaque Monkey. *Journal of neurophysiology* **96**, 3323-3337 (2006). https://doi.org/10.1152/jn.00392.2006
47 Carbajal, G. V. & Malmierca, M. S. The Neuronal Basis of Predictive Coding Along the Auditory Pathway: From the Subcortical Roots to Cortical Deviance Detection. *Trends Hear* **22**, 2331216518784822 (2018). https://doi.org/10.1177/2331216518784822
48 Heilbron, M. & Chait, M. Great Expectations: Is there Evidence for Predictive Coding in Auditory Cortex? *Neuroscience* **389**, 54-73 (2018). https://doi.org/https://doi.org/10.1016/j.neuroscience.2017.07.061
49 Chao, Z. C., Huang, Y. T. & Wu, C. T. A quantitative model reveals a frequency ordering of prediction and prediction-error signals in the human brain. *Commun Biol* **5**, 1076 (2022). https://doi.org/10.1038/s42003-022-04049-6
50 Caucheteux, C., Gramfort, A. & King, J.-R. Evidence of a predictive coding hierarchy in the human brain listening to speech. *Nature Human Behaviour* **7**, 430-441 (2023). https://doi.org/10.1038/s41562-022-01516-2
51 Strube, A., Rose, M., Fazeli, S. & Büchel, C. Alpha-to-beta- and gamma-band activity reflect predictive coding in affective visual processing. *Scientific Reports* **11**, 23492 (2021). https://doi.org/10.1038/s41598-021-02939-z
52 Barron, H. C., Auksztulewicz, R. & Friston, K. Prediction and memory: A predictive coding account. *Prog Neurobiol* **192**, 101821 (2020). https://doi.org/10.1016/j.pneurobio.2020.101821
53 Bastos, André M. *et al.* Visual Areas Exert Feedforward and Feedback Influences through Distinct Frequency Channels. *Neuron* **85**, 390-401 (2015). https://doi.org/10.1016/j.neuron.2014.12.018
54 Sikkens, T., Bosman, C. A. & Olcese, U. The role of top-down modulation in shaping sensory processing across brain states: implications for consciousness. *Frontiers in systems neuroscience* **13**, 31 (2019).
55 Michalareas, G. *et al.* Alpha-beta and gamma rhythms subserve feedback and feedforward influences among human visual cortical areas. *Neuron* **89**, 384-397 (2016).
56 Plakke, B. & Romanski, L. M. Auditory connections and functions of prefrontal cortex. *Frontiers in Neuroscience* **Volume 8 - 2014** (2014). https://doi.org/10.3389/fnins.2014.00199

57 Nourski, K. V. *et al.* Cortical responses to auditory novelty across task conditions: An intracranial electrophysiology study. *Hearing Research* **399**, 107911 (2021). https://doi.org/https://doi.org/10.1016/j.heares.2020.107911

58 Cornella, M., Leung, S., Grimm, S. & Escera, C. Detection of Simple and Pattern Regularity Violations Occurs at Different Levels of the Auditory Hierarchy. *PLOS ONE* **7**, e43604 (2012). https://doi.org/10.1371/journal.pone.0043604

59 Chao, Z. C., Huang, Y. T. & Wu, C.-T. A quantitative model reveals a frequency ordering of prediction and prediction-error signals in the human brain. *Communications Biology* **5**, 1076 (2022). https://doi.org/10.1038/s42003-022-04049-6

60 Hockley, A., Bohórquez, L. H. & Malmierca, M. S. Top-down prediction signals from the medial prefrontal cortex govern auditory cortex prediction errors. *Cell Reports* **44** (2025).

61 Dhamala, M., Rangarajan, G. & Ding, M. Analyzing information flow in brain networks with nonparametric Granger causality. *NeuroImage* **41**, 354-362 (2008). https://doi.org/https://doi.org/10.1016/j.neuroimage.2008.02.020

62 Bressler, S. L. & Seth, A. K. Wiener–Granger Causality: A well established methodology. *NeuroImage* **58**, 323-329 (2011). https://doi.org/https://doi.org/10.1016/j.neuroimage.2010.02.059

63 Auksztulewicz, R. & Friston, K. Repetition suppression and its contextual determinants in predictive coding. *Cortex* **80**, 125-140 (2016). https://doi.org/10.1016/j.cortex.2015.11.024

64 Haenschel, C., Vernon, D. J., Dwivedi, P., Gruzelier, J. H. & Baldeweg, T. Event-related brain potential correlates of human auditory sensory memory-trace formation. *Journal of Neuroscience* **25**, 10494-10501 (2005).

65 Yu, X. J., Xu, X. X., He, S. & He, J. Change detection by thalamic reticular neurons. *Nature Neuroscience* **12**, 1165-1170 (2009). https://doi.org/10.1038/nn.2373

66 Chen, C., Xu, S., Wang, Y. & Wang, X. Location-specific neural facilitation in marmoset auditory cortex. *Nat Commun* **16**, 2773 (2025). https://doi.org/10.1038/s41467-025-58034-8

67 Gill, N. K. & Francis, N. A. Repetition plasticity in primary auditory cortex occurs across long timescales for spectrotemporally randomized pure-tones. *bioRxiv* (2023). https://doi.org/10.1101/2023.04.26.538446

68 Burke, R. *et al.* The role of delta phase for temporal predictions investigated with bilateral parietal tACS. *Brain Stimul* **18**, 103-113 (2025). https://doi.org/10.1016/j.brs.2024.12.1476

69 Majerus, S. *et al.* Cross-Modal Decoding of Neural Patterns Associated with Working Memory: Evidence for Attention-Based Accounts of Working Memory. *Cereb Cortex* **26**, 166-179 (2016). https://doi.org/10.1093/cercor/bhu189

70 Osmanski, M. S. & Wang, X. Behavioral dependence of auditory cortical responses. *Brain Topogr* **28**, 365-378 (2015). https://doi.org/10.1007/s10548-015-0428-4

71 Manea, A. M. G. *et al.* Neural timescales reflect behavioral demands in freely moving rhesus macaques. *Nat Commun* **15**, 2151 (2024). https://doi.org/10.1038/s41467-024-46488-1

72 Recasens, M., Leung, S., Grimm, S., Nowak, R. & Escera, C. Repetition suppression and repetition enhancement underlie auditory memory-trace formation in the human brain: an MEG study. *Neuroimage* **108**, 75-86 (2015).

73 Cacciaglia, R., Costa-Faidella, J., Zarnowiec, K., Grimm, S. & Escera, C. Auditory predictions shape the neural responses to stimulus repetition and sensory change. *Neuroimage* **186**, 200-210 (2019).

74 Vinck, M., Uran, C., Dowdall, J. R., Rummell, B. & Canales-Johnson, A. Large-scale interactions in predictive processing: oscillatory versus transient dynamics. *Trends Cogn Sci* **29**, 133-148 (2025). https://doi.org/10.1016/j.tics.2024.09.013
75 Feldman, H. & Friston, K. J. Attention, uncertainty, and free-energy. *Front Hum Neurosci* **4**, 215 (2010). https://doi.org/10.3389/fnhum.2010.00215
76 Arnal, L. H. & Giraud, A. L. Cortical oscillations and sensory predictions. *Trends Cogn Sci* **16**, 390-398 (2012). https://doi.org/10.1016/j.tics.2012.05.003
77 Wilsch, A., Henry, M. J., Herrmann, B., Maess, B. & Obleser, J. Slow-delta phase concentration marks improved temporal expectations based on the passage of time. *Psychophysiology* **52**, 910-918 (2015). https://doi.org/10.1111/psyp.12413
78 Salimi, M., Tabasi, F., Nazari, M., Ghazvineh, S. & Raoufy, M. R. The olfactory bulb coordinates the ventral hippocampus-medial prefrontal cortex circuit during spatial working memory performance. *J Physiol Sci* **72**, 9 (2022). https://doi.org/10.1186/s12576-022-00833-5
79 Chao, Z. C., Takaura, K., Wang, L., Fujii, N. & Dehaene, S. Large-Scale Cortical Networks for Hierarchical Prediction and Prediction Error in the Primate Brain. *Neuron* **100**, 1252-1266 e1253 (2018). https://doi.org/10.1016/j.neuron.2018.10.004
80 Durschmid, S. *et al.* Hierarchy of prediction errors for auditory events in human temporal and frontal cortex. *Proc Natl Acad Sci U S A* **113**, 6755-6760 (2016). https://doi.org/10.1073/pnas.1525030113
81 Camalier, C. R., Scarim, K., Mishkin, M. & Averbeck, B. B. A Comparison of Auditory Oddball Responses in Dorsolateral Prefrontal Cortex, Basolateral Amygdala, and Auditory Cortex of Macaque. *J Cogn Neurosci* **31**, 1054-1064 (2019). https://doi.org/10.1162/jocn_a_01387
82 Feldman, H. & Friston, K. Attention, Uncertainty, and Free-Energy. *Frontiers in Human Neuroscience* **Volume 4 - 2010** (2010). https://doi.org/10.3389/fnhum.2010.00215
83 Song, P. *et al.* Temporal merging into pitch with click train in the macaque auditory cortex. *National Science Review* (2025). https://doi.org/10.1093/nsr/nwaf026
84 Gong, Y. *et al.* Neural correlates of novelty detection in the primary auditory cortex of behaving monkeys. *Cell Reports* **43**, 113864 (2024). https://doi.org/https://doi.org/10.1016/j.celrep.2024.113864
85 Oostenveld, R., Fries, P., Maris, E. & Schoffelen, J. M. FieldTrip: Open source software for advanced analysis of MEG, EEG, and invasive electrophysiological data. *Comput Intell Neurosci* **2011**, 156869 (2011). https://doi.org/10.1155/2011/156869
86 Rouder, J. N., Speckman, P. L., Sun, D., Morey, R. D. & Iverson, G. Bayesian t tests for accepting and rejecting the null hypothesis. *Psychonomic Bulletin & Review* **16**, 225-237 (2009). https://doi.org/10.3758/PBR.16.2.225
87 Rouder, J. N., Morey, R. D., Speckman, P. L. & Province, J. M. Default Bayes factors for ANOVA designs. *Journal of Mathematical Psychology* **56**, 356-374 (2012). https://doi.org/https://doi.org/10.1016/j.jmp.2012.08.001
88 klabhub/bayesFactor: Bayes only v. v3.0 (Zenodo, 2024).

Acknowledgments

Funding:
STI2030-Major Projects grant 2022ZD0204600 (X.Y.)
STI2030-Major Projects grant 2022ZD0204800 (X.Y.)
National Natural Science Foundation of China grant 32571216 (X.Y.)
National Natural Science Foundation of China grant 32171044 (X.Y.)
National Natural Science Foundation of China grant 32100827 (Y.Z.)

Project PID2023-148541OB-I00, funded by MICIU/AEI (https://doi.org/10.13039/501100011033) and FEDER EU.
The Consejería de Educación, Junta de Castilla y León (SA218P23), and the strategic research programs of excellence from the Regional Government of Castile and León, co-funded by the ERDF Operational Programme (ref. CLU-2023-1-01), awarded to M.S.M.

Author contributions:

Conceptualization: X.Y.
Methodology: X.Y., H.X. and P.S.
Investigation and Data Curation: H.X., P.S., H.Y., Q.Z., X.D. and Y.Z.
Writing-Original Draft: X.Y., H.X., P.S., D.P.G. and M.S.M
Writing-Review & Editing: H.X., P.S., X.Y., A.B.L.R.D.P.G. and M.S.M
Funding Acquisition: X.Y., Y.Z. and M.S.M
Resources: H.T. and X.Y.
Software: H.X., P.S., H.Y., X.B., Y.Z., I.M., Z.T., L.Z. and X.Z.
Validation and Visualization: H.X. and P.S.
Supervision: X.Y., M.S.M.

Competing interests: Authors declare that they have no competing interests.

Data and materials availability: All data are available in the main text or the supplementary materials.

Figures and Tables

Figures are embedded in the main text.

Supplementary Materials

Please use the *Science Advances* template to format your Supplementary Materials.